



Trans. Nonferrous Met. Soc. China 34(2024) 3208-3220

Transactions of Nonferrous Metals Society of China

www.tnmsc.cn



# Microstructural evolution and dynamic recrystallization mechanisms of additively manufactured TiAl alloy with heterogeneous microstructure during hot compression

Hui TAO<sup>1</sup>, Hui-zhong LI<sup>1,2,3</sup>, Jia-hui LI<sup>1</sup>, Li WANG<sup>2</sup>, Wei-wei HE<sup>4</sup>, Xiao-fen TAN<sup>1</sup>, Rui ZHOU<sup>5</sup>, Xiao-peng LIANG<sup>1,2,3</sup>

- 1. School of Materials Science and Engineering, Central South University, Changsha 410083, China;
- 2. State Key Laboratory of Powder Metallurgy, Central South University, Changsha 410083, China;
- 3. Key Laboratory of Nonferrous Metal Materials Science and Engineering, Ministry of Education, Central South University, Changsha 410083, China;
  - 4. Xi'an Sailong AM technologies Co., Ltd., Xi'an 710016, China;
  - 5. Department of Materials Science and Engineering, Hong Kong Institute for Advanced Study, City University of Hong Kong, Kowloon 999077, Hong Kong, China

Received 30 June 2024; accepted 26 September 2024

**Abstract:** Microstructural evolution and dynamic recrystallization (DRX) mechanisms of a Ti-48Al-2Cr-2Nb (at.%) alloy prepared by selective electron beam melting (SEBM) during hot deformation at 1150 °C and 0.1 s<sup>-1</sup> were investigated by hot compression tests, optical microscope (OM), scanning electron microscope (SEM), electron back-scattered diffraction (EBSD) and transmission electron microscope (TEM). The results show that the initial microstructure of the as-SEBMed alloy exhibits layers of coarse  $\gamma$  grains and fine  $\gamma + \alpha_2 + (\alpha_2/\gamma)$  lamellar mixture grains alternately along the building direction. During the early stage of hot deformation, deformation twins tend to form within the coarse grains, facilitating subsequent deformation, and a small number of DRX grains appear in the fine-grained regions. With the increase of strain, extensive DRX grains are formed through different DRX mechanisms in both coarse and fine-grained regions, involving discontinuous dynamic recrystallization mechanism (DDRX) in the fine-grained regions and a coexistence of DDRX and continuous dynamic recrystallization (CDRX) in the coarse-grained regions.

**Key words:** TiAl alloy; selective electron beam melting; heterogeneous microstructure; discontinuous dynamic recrystallization (DDRX); continuous dynamic recrystallization (CDRX)

#### 1 Introduction

 $\gamma$ -TiAl intermetallic compounds have been widely recognized as promising materials for aero engine blades due to their low density, high specific strength, exceptional creep and oxidation resistance at elevated temperatures [1–3]. A typical example is the 4822 alloy (Ti–48Al–2Cr–2Nb (at.%)), which

has been successfully applied in the low-pressure turbine (LPT) blades of the GEnx and LEAP engines [4]. Currently, the TiAl blades are produced through conventional casting or isothermal forging, which is associated with a long production period and limited design flexibility for complex shapes [5,6]. Fortunately, the emergence of the additive manufacturing (AM) has opened up new possibilities, allowing for the direct and precise

production of intricately designed alloy blades. Especially, selective electron beam melting (SEBM) technology stands out as one of the most suitable methods for fabricating brittle TiAl alloys due to its high preheating temperature and low residual stress [7]. Hence, SEBMed  $\gamma$ -TiAl alloys have received considerable attention in recent years [8,9].

However, several defects such as voids and uneven grain distribution are frequently found in AMed products [10,11], which usually need to be eliminated by post-treatment, such as heat treatment [12], hot isostatic pressing (HIP) [13], rolling [14], and forging [15]. As a simple and effective method, hot forging has been applied in many AMed alloys, including Ti-6Al-4V alloy [15,16], Ni-based alloy [17] and stainless steel [18], and has shown significant efficacy in reducing solidification defects and property anisotropy, refining grains, and enhancing mechanical properties. Our previous work [19] also showed the effectiveness of smallstrain forging in synergistically enhancing the strength and ductility of the SEBMed TiAl alloy. To further reveal the deformation mechanism, the thermal compression simulation was utilized under various temperatures and strain rates [20]. However, in actual forging processes, especially in die forging, different positions of the preform are subject to varying levels of strain. Therefore, it is imperative to investigate the influence of strain on the microstructure.

During the hot forging of TiAl alloys, dynamic recrystallization (DRX) is a prominent microstructural characteristic, and the DRX mechanisms include discontinuous dvnamic recrystallization (DDRX) and continuous dynamic recrystallization (CDRX) [21]. DDRX is commonly observed due to its low stacking fault energy (SFE), and it is characterized by grain boundary bulging and migration [22,23]. CDRX involves the continuous transformation of low-angle grain boundaries (LAGBs) into high-angle boundaries (HAGBs) through dislocation cell or sub-grain rotation [24], and it is suggested to be the dominant DRX mode in the  $\alpha_2(\alpha)$  phase [25,26]. The DRX behavior of TiAl alloys is influenced by various factors such as phase composition, initial microstructure, and deformation conditions [27]. For instance, at high strain rate (1 s<sup>-1</sup>), CDRX tends to dominate, while at low strain rate (0.001 s<sup>-1</sup>), DDRX becomes more prevalent [28]. At the early

stage of hot deformation, DDRX serves as the primary nucleation mechanism; with increasing deformation strain, CDRX becomes the dominant mode [29].

In contrast to alloys prepared by traditional methods, the SEBMed 4822 alloy exhibits a typically layered heterogeneous microstructure, characterized by an alternating distribution of coarse and fine grains. This unique microstructure is attributed to the layer-by-layer stacking and prolonged intrinsic annealing during SEBM [30]. Our previous study [20] has revealed distinct DRX behaviors in coarse and fine grains at different strain rates and temperatures during hot deformation. However, the deformation behavior and DRX mechanisms of coarse and fine grains under varying deformation strains have less been elucidated.

Based on the previous research and actual forging conditions, in the present study, the influence of strain on the hot deformation behavior, microstructure evolution and DRX mechanism of TiAl alloy with the heterogeneous microstructure under specific temperature and strain rate was further investigated. This work could provide a valuable theoretical basis for the microstructure control of "AM + hot forging" technology.

#### 2 Experimental

The Ti-48Al-2Cr-2Nb (at.%) pre-alloyed powder produced by the plasma rotating electrode process (PREP) was used for fabricating the TiAl samples on Sailong-Y150 SEBM machine (supplied by Xi'an Sailong AM Technologies Co., Ltd., China). The SEBM parameters are as follows: beam current of 12–15 mA, speed of 3500–4500 mm/s, hatch spacing of 0.1 mm, and preheating temperature of 1100 °C. The snake-like scanning path was adopted in each layer, with a 90° rotation between layers.

Hot compression tests were conducted using a Gleeble–2000D thermo-simulation machine. Cylindrical specimens with a dimension of  $d8 \text{ mm} \times 12 \text{ mm}$  were cut along the building direction (BD) from the as-built alloy, as shown in Fig. 1(a). The target deformation temperature was 1150 °C, the strain rate was  $0.1 \text{ s}^{-1}$ , and the true strain was 0.1, 0.2 and 0.4, respectively. The specimens were heated with a heating rate of 5 °C/s up to

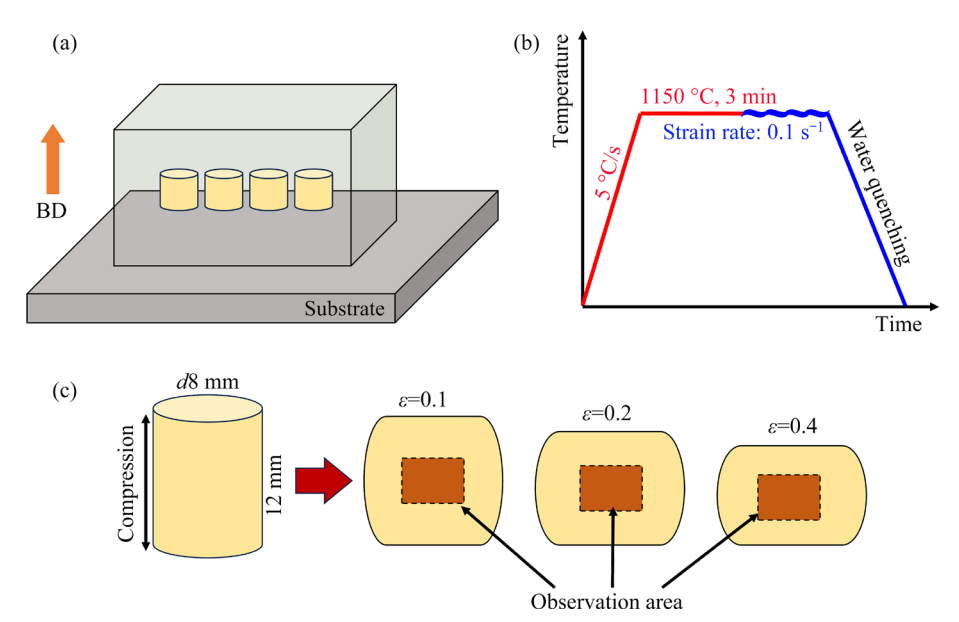


**Fig. 1** Schematic illustrations of experimental process: (a) Sampling preparation; (b) Hot compression test parameters; (c) Sampling location for microstructural characterization

1150 °C and kept for 3 min. After compression, the specimens were water quenched immediately to maintain the deformed microstructure, as shown in Figs. 1(b, c).

The deformed specimens were sliced in half along the compression axis, and the central region of the deformed specimens was selected as the observation area, as shown in Fig. 1(c). The microstructure analysis was conducted using a Leica DMI3000 optical microscope (OM), a TESCAN MIRA3 LMH scanning electron microscope (SEM), an EDAX XM4-Hikari electron backscattered diffraction (EBSD), equipped on the FEI SIRION 200 SEM (voltage of 25 kV, working distance of 9 mm, and scanning step of 0.15 µm), as well as a FEI Tecnai G2 F20 transmission electron microscope (TEM). EBSD data analyses were carried out on TSL-OIM software. The samples for SEM and EBSD tests were prepared by grinding and electrochemically polishing in an electrolyte solution consisting of 6% perchloric acid, 34% butanol, and 60% methanol. TEM samples were ground into thin slices with a thickness of about 60 μm, and then thinned using a RL-I twin-jet electropolishing machine at 25 V and -30 °C.

#### 3 Results

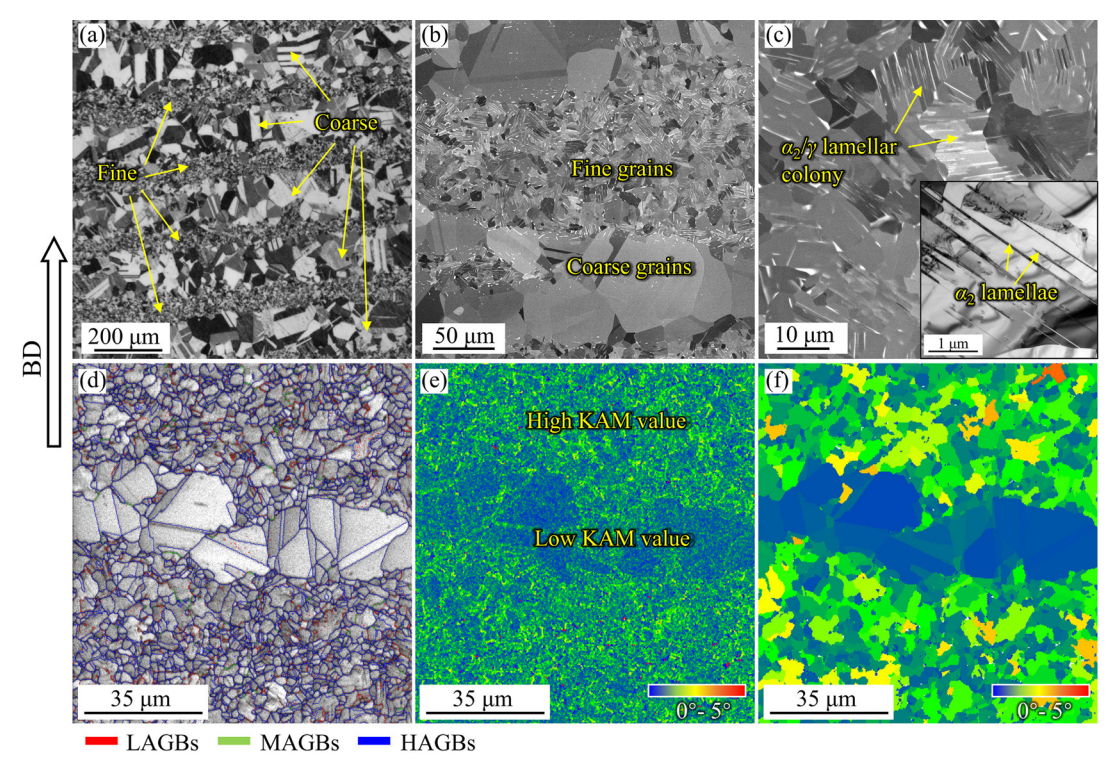
#### 3.1 Initial microstructure

Figure 2 presents the microstructure of the as-SEBMed Ti-48Al-2Cr-2Nb alloy before hot

compression. The microstructure demonstrates alternating layers of coarse grains and fine grains along the build direction (BD) (Fig. 2(a)). The coarse grains consist of a single  $\gamma$  phase, while the fine grains consist of numerous γ phase, a small amount  $\alpha_2$  phase and  $\alpha_2/\gamma$  lamellar colonies (Fig. 2(b)). The  $\alpha_2/\gamma$  lamellar colonies are observed to be degraded, characterized by decomposed  $\alpha_2$ lamellae, as shown in Fig. 2(c). Additionally, many annealing twins are formed within the coarse  $\gamma$ grains. The image quality (IQ) map overlapped grain boundary distribution map (Fig. 2(d)) exhibits that the fractions of the low-angle grain boundaries (LAGBs, 2°-10°), middle-angle grain boundaries (MAGBs,  $10^{\circ}-15^{\circ}$ ), and high-angle boundaries (HAGBs, >15°) are 18.5%, 2.3%, 79.2%, respectively, and all boundaries of coarse grains belong to HAGBs. The corresponding KAM map (Fig. 2(e)) indicates that high KAM values predominantly exist within fine grains and at grain boundaries. The KAM value, which represents the geometrically necessary dislocation (GND) density of alloys [31], implies a higher GND in these areas compared to coarse-grained regions. Grain orientation spread (GOS) maps (Fig. 2(f)) also indicate higher lattice distortion and a larger number of local disorientations in fine-grained regions.

#### 3.2 Flow behavior

The true stress-true strain curves of the as-SEBMed Ti-48Al-2Cr-2Nb alloy under different



**Fig. 2** Microstructures of as-SEBMed Ti-48Al-2Cr-2Nb alloy before hot compression deformation: (a) OM image; (b) SEM image at low magnification; (c) Magnified SEM image in fine-grained region and TEM image inserted in lower right corner; (d) IQ map overlapped grain boundary distribution map; (e) KAM map; (f) GOS map

strains are displayed in Fig. 3. The flow stress exhibits a rapid increase in the elastic region and then reaches a peak stress of 349 MPa. Subsequently, with increasing strain, the flow stress gradually decreases until it reaches the final strain. This phenomenon is a common characteristic in TiAl alloys during the hot deformation [32,33]. At the initial stage of deformation, the flow stress curves exhibit the characteristics of obvious work hardening, which is attributed to the significant dislocation multiplication. As the dislocation density further increases, dislocation pile-ups promote the nucleation of DRX grains. With continued strain accumulation, DRX grains nucleate and grow and dislocations are absorbed, resulting in a gradual decrease in flow stress [34]. It is worth noting that the flow stress initially decreases after reaching the peak value, followed by a sudden increase and ultimately a gradual decrease. This phenomenon is attributed to the interaction between work hardening and DRX.

### 3.3 Microstructure evolution during hot compression

Electron channeling contrast images (ECCI) in

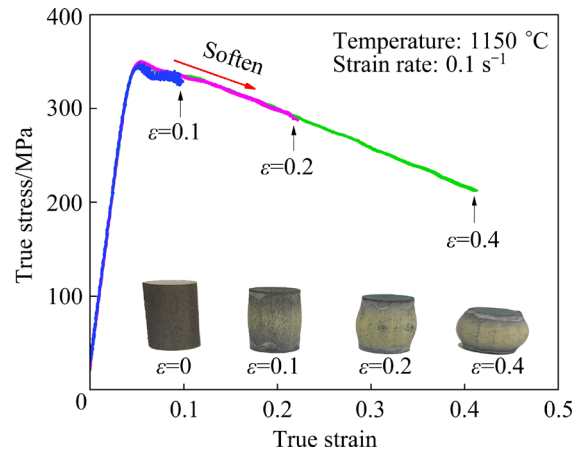


Fig. 3 Flow stress curves and macroscopic morphologies of samples

Fig. 4 illustrate the microstructural evolution of the deformed samples under varying strains. With increasing strain, a gradual refinement of grains is observed (Figs. 4(a-c)). The flattened shape of coarse grains becomes more pronounced as strain increases, and particularly evident at a true strain of 0.4, the white  $\alpha_2$  phase in fine-grained regions elongates significantly along the direction perpendicular to the compression. Enlarged view images at the coarse/fine grain interface reveal an

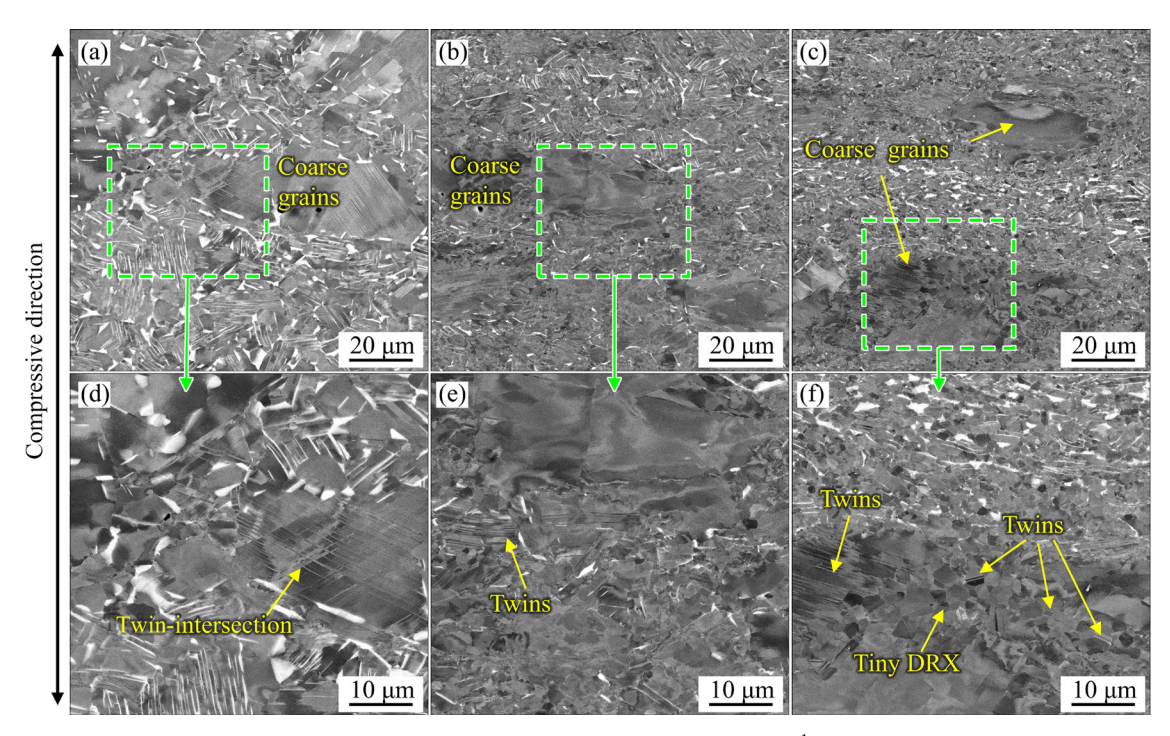
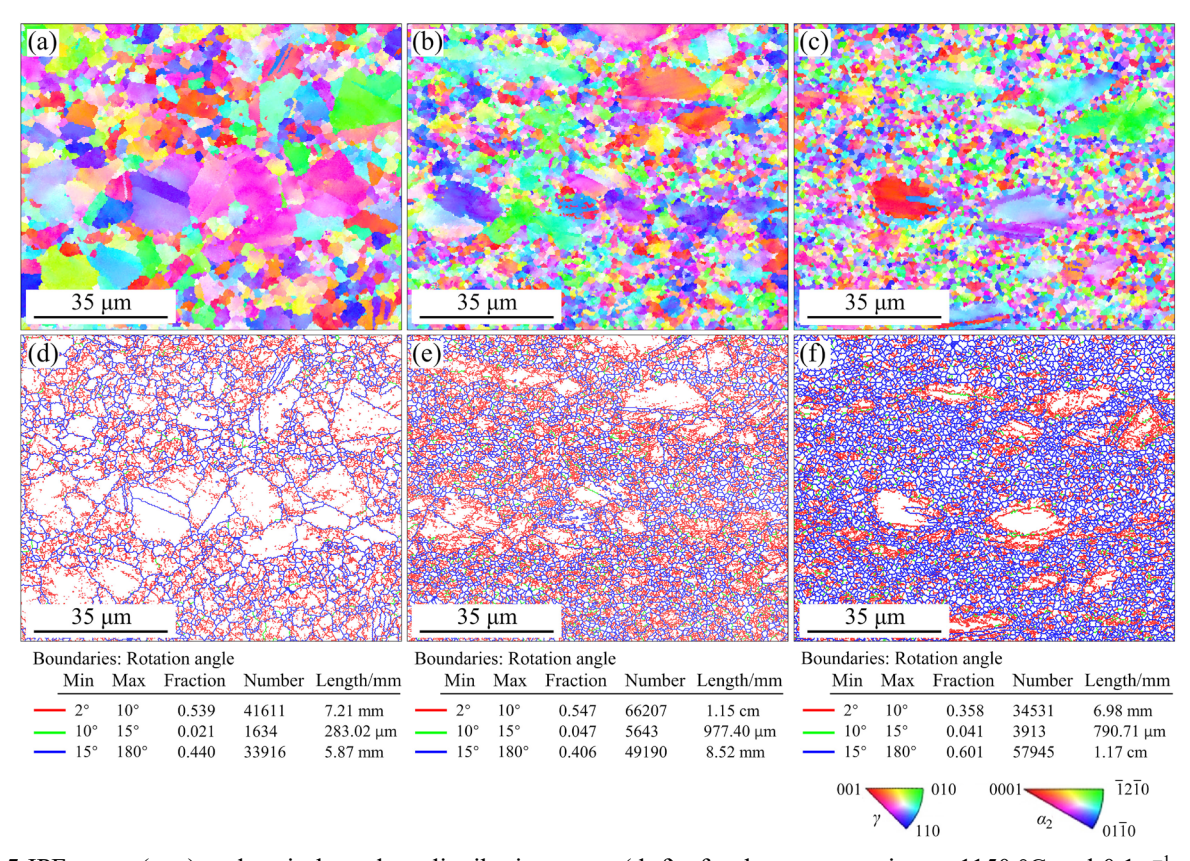


Fig. 4 ECCI images of samples after hot compression at 1150 °C and 0.1 s<sup>-1</sup> under various true strains: (a, d) 0.1; (b, e) 0.2; (c, f) 0.4

abundant generation of deformation twins within the coarse grains (Figs. 4(d-f)). At a true strain of 0.1, there is a high density of deformation twin intersections (Fig. 4(d)). However, with an increase in true strain to 0.2 and 0.4, the deformation twins appear to diminish and some twin boundaries exhibit bending (Figs. 4(e, f)). It is noteworthy that at a true strain of 0.4, numerous tiny DRX grains are generated within and surrounding the coarse grains, with observable twins within these DRX grains (Fig. 4(f)).

The IPF maps and the corresponding grain boundary distribution maps of the samples after hot compression at 1150 °C and 0.1 s<sup>-1</sup> under various strains are shown in Fig. 5. With increasing strain, the proportion of coarse grains decreases, and these grains gradually compress and elongate, which is consistent with SEM observations. Compared to the original microstructure (Fig. 2(e)), the fractions of LAGBs and MAGBs significantly increase after hot compression at a true strain of 0.1 (Fig. 5(d)). As the true strain increases from 0.1 to 0.2, the fractions of LAGBs and MAGBs increase slightly, and specifically, LAGBs increase from 53.9% to 54.7% and MAGBs increase from 2.1% to 4.7%. Accordingly, the fractions of HAGBs decrease from 44.6% to 40.6%. Notably, the total length of grain boundaries significantly increases, indicating an obvious refinement in microstructure, as observed in Fig. 5(e). When the true strain reaches 0.4, the fractions of HAGBs increase significantly, reaching 60.1% (Fig. 5(f)). However, the total grain boundary length remains relatively unchanged, which is primarily attributed to the transformation from LAGBs to HAGBs. Besides, a substantial amount of LAGBs and MAGBs are observed around and within the coarse grains.

The KAM maps and GOS maps of the samples after hot compression at 1150 °C and 0.1 s<sup>-1</sup> under various true strains are depicted in Fig. 6. The KAM maps (Figs. 6(a-c)) reveal a significantly higher KAM value in the deformed alloy compared to the initial alloy (Fig. 2(e)). Furthermore, at a true strain of 0.1, the KAM value in coarse grains remains lower than that in fine grains. However, as the strain increases to 0.2 and 0.4, the coarse grains exhibit higher KAM values, indicating distinct changes in dislocation density between coarse and fine grains with increasing strain. Besides, GOS maps are commonly utilized to distinguish DRX grains from deformed grains [35]. Regions with lower GOS values indicate the characteristics of DRX grains. As strain increases (Figs. 6(d-f)), the blue area (indicative of low GOS value) becomes



**Fig. 5** IPF maps (a–c) and grain boundary distribution maps (d–f) after hot compression at 1150 °C and 0.1 s<sup>-1</sup> under various true strains: (a, d) 0.1; (b, e) 0.2; (c, f) 0.4

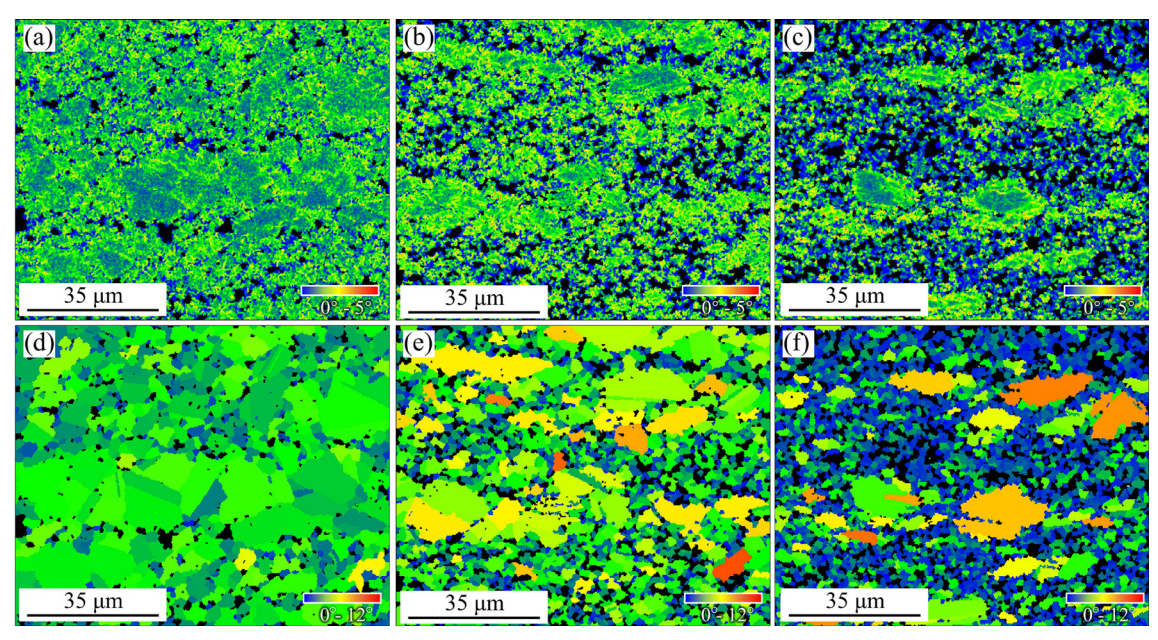


**Fig. 6** Kernel average misorientation (KAM) maps (a-c) and grain orientation spread (GOS) maps (d-f) after hot compression at 1150 °C and 0.1 s<sup>-1</sup> under various true strains: (a, d) 0.1; (b, e) 0.2; (c, f) 0.4

more extensive, suggesting a greater extent of recrystallization. Meanwhile, there is a significant increase in the GOS value in coarse grains, also indicating severe plastic deformation in these

regions.

Furthermore, the critical GOS value ( $\leq 2^{\circ}$ ) is usually utilized to distinguish and quantify DRX grains in TiAl alloys [36]. As depicted in Fig. 7, the

distribution of DRX grains primarily occurs in the fine-grained regions. With an increase in true strain from 0.1 to 0.2, the volume fraction of DRX grains slightly increases from 19.6% to 19.9%, accompanied by a significant decrease in the mean grain size of DRX grains from 3.0 to 1.5  $\mu$ m. Subsequently, when the true strain further increases to 0.4, the volume fraction of DRX grains increases sharply, reaching 43.6%, while the average grain size does not change.

Figure 8 presents the TEM microstructure of the samples after hot compression at 1150 °C and 0.1 s<sup>-1</sup> under the true strain of 0.1. The HAADF image in Fig. 8(a) reveals that the microstructure predominantly consists of  $\gamma$  grains, exhibiting a significant twinning within these grains. The magnified bright-field image (Fig. 8(b)) shows that deformation twins tend to nucleate at interface and propagate across  $\gamma$  grains, terminating at another interface. Meanwhile, dislocations are confined to the subdistricts divided by the deformation twins. The presence of deformation twins is further confirmed by the selected area diffraction pattern recorded along the  $\langle 101 \rangle_{\nu}$  direction (bottom right corner of Fig. 8(b)). Additionally, a high-density deformation twin intersection is observed (Fig. 8(c)). The presence of twins-intersection further divides the matrix into subdistricts and

greatly limits the mobility of dislocation. Upon further magnification (Fig. 8(d)), severe dislocation entanglement exists at the twin boundary, and numerous sub-structures are formed in the twinsintersection regions, which are conducive to DRX grain nucleation [37].

The TEM microstructures of samples after hot compression at 1150 °C and 0.1 s<sup>-1</sup> under the true strains of 0.2 and 0.4 are depicted in Figs. 9 and 10, respectively. The HAADF image of Fig. 9(a) reveals high-density dislocations in the alloy. The continuous accumulation of dislocations in the interior of the deformed grains results in the appearance of high-density dislocation regions, and the formation of entangled dislocations (Fig. 9(b)) and dislocation walls (DWs) (Fig. 9(c)). Besides, numerous sub-structures can be observed, which are distributed from the inside of the grain to adjacent grain boundary. After undergoing further deformation to a true strain of 0.4 (Fig. 10), extensive DRX grains are observed, accompanied by a reduction in dislocation density to some extent (Fig. 10(a)). Twins can be observed within the newly formed DRX grain (Fig. 10(b)). These tiny DRX grains predominantly distribute near grain boundaries, exhibiting a typical characteristic of discontinuous dynamic recrystallization (DDRX) (Figs. 10(b, c)).

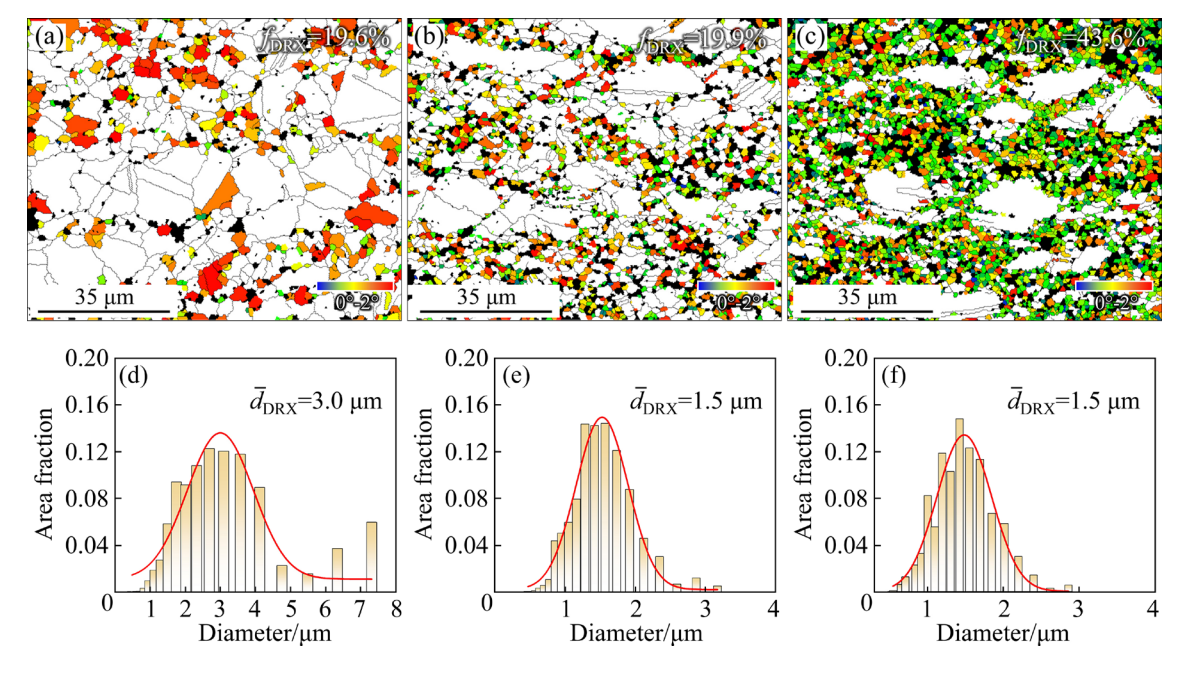


**Fig. 7** Distribution of recrystallization grains (a–c) and DRX grain size statistics (d–f) after hot compression at 1150 °C and 0.1 s<sup>-1</sup> under various true strains: (a, d) 0.1; (b, e) 0.2; (c, f) 0.4

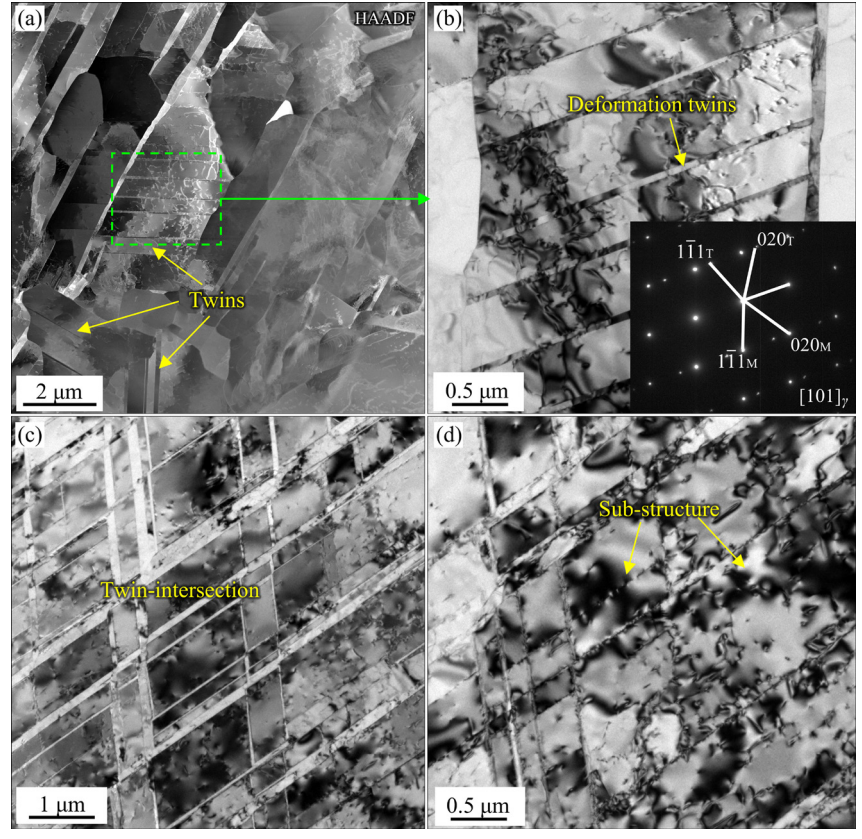


Fig. 8 HAADF image (a) and bright-field images (b-d) after hot compression at  $1150 \, ^{\circ}\text{C}$  and  $0.1 \, \text{s}^{-1}$  under true strain of 0.1

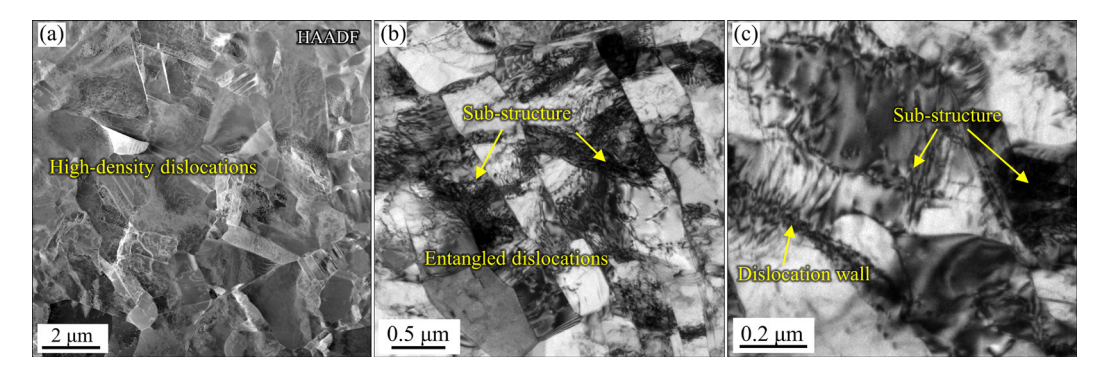


Fig. 9 HAADF image (a) and bright-field images (b, c) after hot compression at  $1150 \, ^{\circ}\text{C}$  and  $0.1 \, \text{s}^{-1}$  under true strain of 0.2

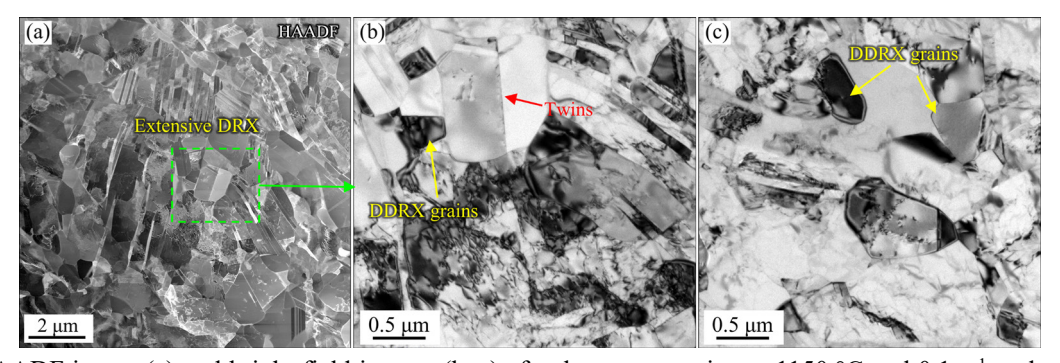


Fig. 10 HAADF image (a) and bright-field images (b, c) after hot compression at  $1150~^{\circ}\text{C}$  and  $0.1~\text{s}^{-1}$  under true strain of 0.4

#### 4 Discussion

Generally, the flow stress curves of the alloys reflect their deformation mechanical behavior, as well as provide insights into the trend of microstructural evolution [38]. During the initial stages of deformation, there is a rapid increase in flow stress due to a sharp increase in dislocation density. When a balance between work hardening and dynamic softening is achieved, the flow stress reaches its peak. As deformation continues, the softening mechanism takes effect. DRX grains nucleate and grow, dislocations are absorbed, and the flow stress gradually decreases. Consequently, at a true strain of 0.1, the number and the length of LAGBs increase significantly, and only a small number of DRX grains are observed. With an increase in true strain to 0.2 and 0.4, the LAGB network evolves into more regular sub-structures, some LAGBs transform into HAGBs, DRX behavior becomes prevalent. Notably, hot deformation leads to the formation of numerous deformation twins, particularly at a true strain of 0.1, where twin-intersection is frequently observed. The occurrence of deformation twins compensates for the lack of independent glide systems, promoting the coordination deformation, while causing significant work hardening [39]. Thus, the sudden increase in stress at a true strain of about 0.07 during the softening of the flow stress curve (Fig. 3) is attributed to the formation of deformation twins.

On the other hand, the deformation behavior of heterogeneous microstructures exhibits distinct characteristics during the hot deformation process, which is closely related to the different deformability of coarse and fine grains. The coarse grains consist of single  $\gamma$  phases and belong to the soft domains [20]; thus, they preferentially yield during hot compression, and exhibit a flat grain morphology. Moreover, larger grains not only provide sufficient space for continuous dislocation slip but also facilitate the formation development of deformation twins [40]. Under the deformation rate of 0.1 s<sup>-1</sup> in this study, the release of stress concentration is difficult for coarse grains through grain rotation and dislocation motion in a short period of time. Consequently, during the early stage of hot deformation, deformation twins tend to form in the coarse grains to facilitate the subsequent deformation. As strain increases, a significant accumulation of dislocations occurs near the grain boundaries of coarse grains. As mentioned previously, DDRX usually originates from the unbalanced dislocation density on both sides of the grain boundary, and the grain boundary tends to migrate towards the side with higher dislocation density [41]. Subsequently, sub-grain boundaries are developed at the original grain boundary and further transform into DDRX nuclei. As depicted in Fig. 11, the serrated boundaries are observed along the coarse grain, which is the result of the bulging of grain boundaries. Therefore, it can be inferred that the DRX mechanism around the boundary of coarse grains is DDRX.

Moreover, a larger grain size significantly increases the distance between the dislocation source and grain boundary [42]. As a result, a higher dislocation density can readily be accommodated within the coarse grains, which is conducive to the dislocation rearrangement and entanglement, resulting in formation of dislocation cells and sub-grains, and further transform into

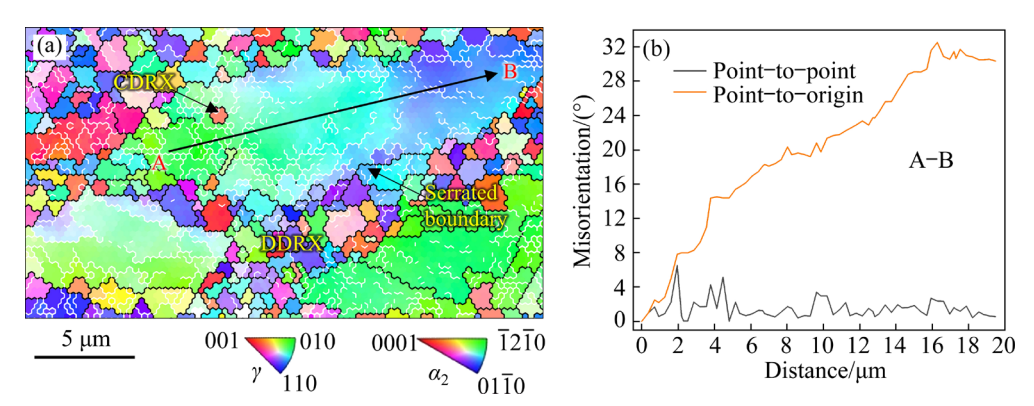


Fig. 11 IPF map (a) and misorientation angle along A-B line (b) of coarse grains selected from sample deformed at true strain of 0.4

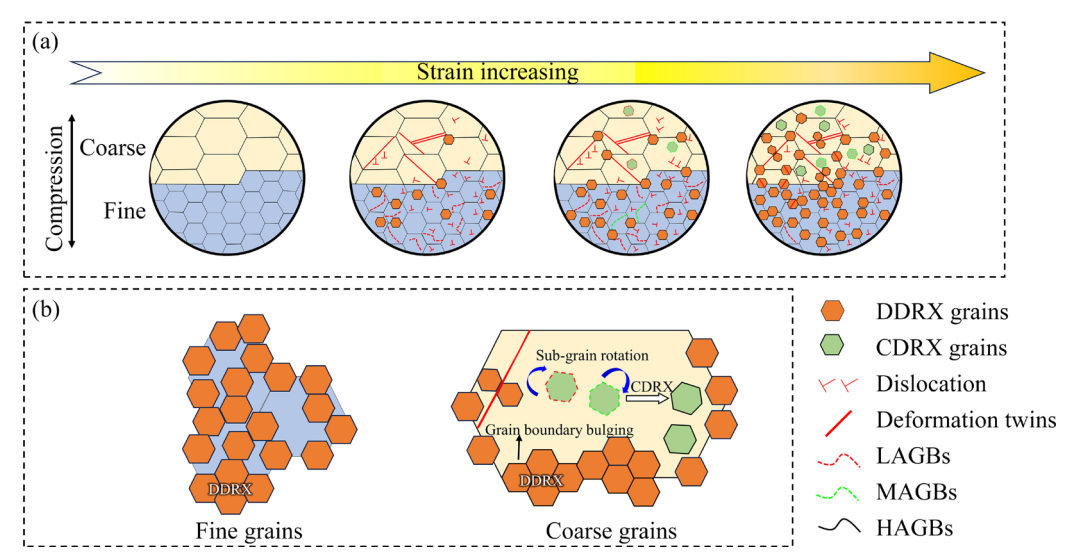


Fig. 12 Schematic illustrations showing microstructural evolution (a) and DRX mechanisms (b) of as-SEBMed TiAl alloys with heterogeneous microstructure during hot compression process

CDRX grains. Since the CDRX process is caused by the progressive rotation of sub-grains, original grains typically display a discernible misorientation gradient from the center to the edge [43]. As depicted in Fig. 11, the misorientation along the black arrow A–B exhibits a stepwise rise trend with values exceeding 15°. This continuous accumulation of orientations from point to origin represents a distinctive characteristic of CDRX. Finally, the finer DDRX and CDRX grains gradually replace the coarser deformed grains.

In fine-grained regions, dislocations primarily accumulate at grain boundary due to the finer grain size and higher grain boundary density, facilitating the occurrence of DRX at grain boundaries, which are preferred sites for DDRX nucleation [44]. Thus, the DRX mechanism in fine-grained regions is DDRX.

In summary, the deformation behavior and DRX mechanisms of the heterogeneous as-SEBMed TiAl alloys during the hot compression process are illustrated in Fig. 12. During the initial stage of deformation, the dislocation density increases rapidly within the alloy. Deformation twins are formed within the coarse grains, while a small number of DRX grains are formed in the fine-grained regions. As deformation progresses, the number of DRX grains increases in the fine-grained regions, and some DRX also occurs within the coarse grains. Subsequent deformation results in the widespread distribution of DRX grains, accompanied by new DRX grains exhibiting

deformation twinning as well (Fig. 12(a)). The DRX mechanism in fine-grained regions is primarily DDRX, while the DRX mechanisms in the coarse-grained regions involve a coexistence of DDRX and CDRX (Fig. 12(b)).

#### **5 Conclusions**

- (1) With the increase of true strain, the degree of DRX in the fine-grained regions of as-SEBMed TiAl alloy gradually increases. In coarse-grained regions, a significant number of deformation twins occur at low strains, and DRX is observed at high strains.
- (2) The DRX mechanism in the fine-grained regions is characterized by discontinuous dynamic recrystallization (DDRX), occurring through grain boundary bulging and migration.
- (3) The DRX mechanisms in the coarse-grained regions involve a coexistence of DDRX and CDRX characterized by continuous sub-grain rotation.

#### **CRediT** authorship contribution statement

Hui TAO: Formal analysis, Investigation, Methodology, Writing — Original draft, Writing — Review & editing; Hui-zhong LI: Resources, Supervision, Writing — Review & editing; Jia-hui LI: Methodology; Li WANG: Writing — Review & editing; Wei-wei HE: Methodology, Resources; Xiao-fen TAN: Writing — Review & editing; Rui ZHOU: Writing — Review & editing; Xiao-peng LIANG: Formal analysis,

Methodology, Resources, Supervision, Writing – Review & editing.

#### **Declaration of competing interest**

The authors declare that they have no known competing financial interests or personal relationships that could have appeared to influence the work reported in this paper.

#### Acknowledgments

The authors are grateful for the financial supports from the Shaanxi Province Key Research and Development Projects, China (No. 2023KXJ-071), and the National Natural Science Foundation of China (Nos. 52274402, 52174381).

#### References

- CLEMENS H, KESTLER H. Processing and applications of intermetallic γ-TiAl-based alloys [J]. Advanced Engineering Materials, 2000, 2(9): 551–570.
- [2] APPEL F, PAUL J D H, OEHRING M. Gamma titanium aluminide alloys: Science and technology [M]. Weinheim: Wiley-VCH, 2011.
- [3] ZHENG Guo-ming, TANG Bin, ZHAO Song-kuan, WANG W Y, CHEN Xiao-fei, ZHU Lei, LI Jin-shan. Evading the strength-ductility trade-off at room temperature and achieving ultrahigh plasticity at 800 °C in a TiAl alloy [J]. Acta Materialia, 2022, 225: 117585.
- [4] BEWLAY B P, NAG S, SUZUKI A, WEIMER M J. TiAl alloys in commercial aircraft engines [J]. Materials at High Temperatures, 2016, 33(4/5): 549–559.
- [5] AGUILAR J, SCHIEVENBUSCH A, KÄTTLITZ O. Investment casting technology for production of TiAl low pressure turbine blades-process engineering and parameter analysis [J]. Intermetallics, 2011, 19(6): 757–761.
- [6] JANSCHEK P. Wrought TiAl blades [J]. Materials Today: Proceedings, 2015, 2: S92–S97.
- [7] YUE Hang-yu, PENG Hui, MIAO Ke-song, GAO Bo-yang, WU Hao, YANG Ji-bang, FAN Guo-hua. Significant enhancement in high-temperature tensile strength of trace nano-Y<sub>2</sub>O<sub>3</sub>-reinforced TiAl alloy prepared by selective electron beam melting [J]. Materials Science and Engineering A, 2023, 875: 145086.
- [8] GAO R, PENG H, GUO H, CHEN B. An innovative way to fabricate γ-TiAl blades and their failure mechanisms under thermal shock [J]. Scripta Materialia, 2021, 203: 114092.
- [9] LIU Nan, NIU Jing-zhe, CHEN Yang, WANG Xiang-hui, WANG Jian, XIANG Heng-gao, WEI Dai-xiu, CHEN Guang. Effect of in-situ post-heating on the microstructure and tensile performance of TiAl alloys produced via selective electron beam melting [J]. Materials Science and Engineering A, 2023, 885: 145585.
- [10] DEBROY T, WEI H L, ZUBACK J S, MUKHERJEE T, ELMER J W, MILEWSKI J O, BEESE A M, WILSON-HEID A, DE A, ZHANG W. Additive manufacturing of metallic components-process, structure and properties [J].

- Progress in Materials Science, 2018, 92: 112-224.
- [11] GUO Yu, CHEN Chao, WANG Qiang-bing, LIU Min, CAO Yuan-kui, PAN Yan-ming, TAN Li-ming. Effect of porosity on mechanical properties of porous tantalum scaffolds produced by electron beam powder bed fusion [J]. Transactions of Nonferrous Metals Society of China, 2022, 32(9): 2922–2934.
- [12] WANG Lin, SHEN Chen, ZHANG Yue-long, LI Fang, DING Yu-han, ZHOU Wen-lu, XIN Jian-wen, WANG Bao-sen, HUA Xue-ming. Investigation on heat treatment strategy eliminating heterogeneity and anisotropy of TiAl alloy fabricated using twin-wire directed energy depositionarc [J]. Materials Characterization, 2022, 193: 112321.
- [13] SEIFI M, SALEM A A, SATKO D P, ACKELID U, SEMIATIN S L, LEWANDOWSKI J J. Effects of HIP on microstructural heterogeneity, defect distribution and mechanical properties of additively manufactured EBM Ti-48Al-2Cr-2Nb [J]. Journal of Alloys and Compounds, 2017, 729: 1118-1135.
- [14] DONOGHUE J, ANTONYSAMY A A, MARTINA F, COLEGROVE P A, WILLIAMS S W, PRANGNELL P B. The effectiveness of combining rolling deformation with wire-arc additive manufacture on β-grain refinement and texture modification in Ti-6Al-4V [J]. Materials Characterization, 2016, 114: 103–114.
- [15] MA Jian-kai, ZHANG Ya-shan, LI Jun-jie, CUI Ding-cong, WANG Zhi-jun, WANG Jin-cheng. Microstructure and mechanical properties of forging-additive hybrid manufactured Ti-6Al-4V alloys [J]. Materials Science and Engineering A, 2021, 811: 140984.
- [16] MAURYA A K, YEOM J, KANG S W, PARK C H, HONG J, REDDY N S. Optimization of hybrid manufacturing process combining forging and wire-arc additive manufactured Ti-6Al-4V through hot deformation characterization [J]. Journal of Alloys and Compounds, 2022, 894: 162453.
- [17] BAMBACH M, SIZOVA I, SILZE F, SCHNICK M. Hot workability and microstructure evolution of the nickel-based superalloy Inconel 718 produced by laser metal deposition [J]. Journal of Alloys and Compounds, 2018, 740: 278–287.
- [18] PRUNCU C I, HOPPER C, HOOPER P A, TAN Z, ZHU H, LIN J, JIANG J. Study of the effects of hot forging on the additively manufactured stainless steel preforms [J]. Journal of Manufacturing Processes, 2020, 57: 668–676.
- [19] TAO Hui, LI Hui-zhong, WANG Li, CHE Yi-xuan, HE Wei-wei, LI Hui-xia, ZHOU Rui, LIANG Xiao-peng. Improvement on high-temperature tensile strength and ductility of selective electron beam melting TiAl alloys via small-strain forging [J]. Materials Science and Engineering A, 2023, 873: 145009.
- [20] TAO Hui, LI Hui-zhong, ZHOU Rui, HE Wei-wei, LI Hui-xia, CHE Yi-xuan, LI Ling, WANG Li, LIANG Xiao-peng. Hot deformation behavior of a layered heterogeneous microstructure TiAl alloy prepared by selective electron beam melting [J]. Materials Characterization, 2024, 212: 113986.
- [21] YUAN Cheng-hao, LIU Bin, LIU Yu-xi, LIU Yong. Processing map and hot deformation behavior of Ta-particle reinforced TiAl composite [J]. Transactions of Nonferrous Metals Society of China, 2020, 30(3): 657–667.

- [22] WAN Zhi-peng, SUN Yu, HU Lian-xi, YU Huan. Experimental study and numerical simulation of dynamic recrystallization behavior of TiAl-based alloy [J]. Materials & Design, 2017, 122: 11–20.
- [23] LI Jian-bo, LIU Yong, WANG Yan, LIU Bin, HE Yue-hui. Dynamic recrystallization behavior of an as-cast TiAl alloy during hot compression [J]. Materials Characterization, 2014, 97: 169–177.
- [24] YANG Jun-zhou, WU Jian-jun, XIE Hai-nan, LI Zhi-guo, WANG Kai-wei. Mechanism of continuous dynamic recrystallization of Ti-6Al-4V alloy during superplastic forming with sub-grain rotation [J]. Transactions of Nonferrous Metals Society of China, 2023, 33(3): 777-788.
- [25] LI Juan, LI Ming-ao, HU Li, SHI Lai-xin, XIAO Shu-long, CHEN Yu-yong, ZHOU Tao. Dynamic recrystallization, phase transformation and deformation mechanisms of a novel Ti-43Al-6Nb-1Mo-1Cr alloy during the isothermal deformation [J]. Materials Characterization, 2023, 199: 112789.
- [26] XU R R, LI H, LI M Q. Dynamic recrystallization mechanism of  $\gamma$  and  $\alpha$  phases during the isothermal compression of  $\gamma$ -TiAl alloy with duplex structure [J]. Journal of Alloys and Compounds, 2020, 844: 156089.
- [27] SINGH V, MONDAL C, SARKAR R, BHATTACHARJEE P P, GHOSAL P. Dynamic recrystallization of a β(B2)-stabilized γ-TiAl based Ti-45Al-8Nb-2Cr-0.2B alloy: The contributions of constituent phases and Zener-Hollomon parameter modulated recrystallization mechanisms [J]. Journal of Alloys and Compounds, 2020, 828: 154386.
- [28] CHEN Yuan-yu, LI Lian, LI Hong, LI Miao-quan. Dynamic recrystallization mechanism and twinning behavior in hot deformation of Ti-46.5Al-2Nb-2Cr with initial duplex microstructure [J]. Materials Characterization, 2023, 197: 112678.
- [29] WANG Gang, XU Lei, TIAN Yu-xing, ZHENG Zhuo, CUI Yu-you, YANG Rui. Flow behavior and microstructure evolution of a P/M TiAl alloy during high temperature deformation [J]. Materials Science and Engineering A, 2011, 528: 6754–6763.
- [30] WARTBICHLER R, CLEMENS H, MAYER S, GHIBAUDO C, RIZZA G, GALATI M, IULIANO L, BIAMINO S, UGUES D. On the formation mechanism of banded microstructures in electron beam melted Ti-48Al-2Cr-2Nb and the design of heat treatments as remedial action [J]. Advanced Engineering Materials, 2021, 23(12): 2101199.
- [31] ZHU Lei, LI Jin-shan, TANG Bin, ZHAO Feng-tong, HUA Ke, YAN Shao-peng, KOU Hong-chao. Dynamic recrystallization and phase transformation behavior of a wrought  $\beta$ - $\gamma$  TiAl alloy during hot compression [J]. Progress in Natural Science: Materials International, 2020, 30(4): 517–525.
- [32] YANG Wei-gang, LI Ming-ao, ZHOU Tao, HU Li, SHI Lai-xin, XIAO Shu-long, CHEN Yu-yong. Deformation behavior and dynamic recrystallization mechanism of a novel high Nb containing TiAl alloy in (α+γ) dual-phase field [J]. Journal of Alloys and Compounds, 2023, 945: 169250.
- [33] LI Hui-zhong, ZENG Min, LIANG Xiao-peng, LI Zhou, LIU Yong. Flow behavior and processing map of PM Ti-47Al-2Cr-0.2Mo alloy [J]. Transactions of Nonferrous

- Metals Society of China, 2012, 22(4): 754-760.
- [34] YANG Jie-ren, GAO Zi-tong, LIANG Yong-feng, WU Yu-lun, LI Jin-guang, HU Rui. Microstructure refinement assisted by α-recrystallization in a peritectic TiAl alloy [J]. Journal of Materials Research and Technology, 2021, 11: 1135–1141.
- [35] DENG Ying, ZHU Xin-wen, LAI Yi, GUO Yi-fan, FU Le, XU Guo-fu, HUANG Ji-wu. Effects of Zr/(Sc+Zr) microalloying on dynamic recrystallization, dislocation density and hot workability of Al-Mg alloys during hot compression deformation [J]. Transactions of Nonferrous Metals Society of China, 2023, 33(3): 668-682.
- [36] CHEN Xiao-fei, TANG Bin, LIU Dong, WEI Bei-bei, ZHU Lei, LIU Rui-ci, KOU Hong-chao, LI Jin-shan. Dynamic recrystallization and hot processing map of Ti-48Al-2Cr-2Nb alloy during the hot deformation [J]. Materials Characterization, 2021, 179: 111332.
- [37] LIANG Zhen-quan, XIAO Shu-long, LI Xin-yi, CHI Da-zhao, ZHENG Yun-fei, XU Li-juan, XUE Xiang, TIAN Jing, CHEN Yu-yong. Significant improvement in creep resistance of Ti-46Al-6Nb-1Cr-1.5V alloy via introducing high-density nanotwins [J]. Materials Science and Engineering A, 2023, 862: 144485.
- [38] TIAN Shi-wei, JIANG Hai-tao, GUO Wen-qi, ZHANG Gui-hua, ZENG Shang-wu. Hot deformation and dynamic recrystallization behavior of TiAl-based alloy [J]. Intermetallics, 2019, 112: 106521.
- [39] TAO Hui, LIANG Xiao-peng, CHE Yi-xuan, ZHOU Rui, WANG Li, LI Hui-zhong. Optimization of hot-rolling parameters for a powder metallurgy Ti-47Al-2Cr-2Nb-0.2W alloy based on processing map and microstructure evolution [J]. Journal of Materials Research and Technology, 2024, 30: 7284-7294.
- [40] DORAISWAMY D, ANKEM S. The effect of grain size and stability on ambient temperature tensile and creep deformation in metastable beta titanium alloys [J]. Acta Materialia, 2003, 51: 1607–1619.
- [41] JIA Zhi, WEI Bao-lin, SUN Xuan, JI Jin-jin, WANG Yan-jiang, YU Li-dan. Hot workability and dynamic recrystallization mechanisms of pure nickel N6 [J]. Transactions of Nonferrous Metals Society of China, 2022, 32(10): 3259–3275.
- [42] WANG Zhi-qi, CUI Xi-ping, CHEN Ling-fei, ZHANG Yi-fan, DING Hao, ZHANG Yuan-yuan, GAO Nao-nao, CONG Guang-hui, AN Qi, WANG Shuai, CHEN Jun-feng, GENG Lin, HUANG Lu-jun. Achieving superior strength-ductility synergy in a unique multi-scale heterostructured titanium laminate fabricated by temperature-controlled rolling and subsequent annealing [J]. Materials Science and Engineering A, 2024, 891: 145926.
- [43] HU Qing, WANG Yan, LV Liang-xing, LUO Yao-feng, SU Liang, LIU Bin. Hot deformation behavior and dynamic recrystallization mechanism of Ti–48Al–2Nb–2Cr alloy with near-γ microstructure [J]. Journal of Alloys and Compounds, 2023, 945: 169378.
- [44] LU Tong, DAN Zhen-hua, LI Kai, YI Dan-qing, ZHOU Lian, CHANG Hui. Hot deformation behaviors and dynamic recrystallization mechanism of Ti-35421 alloy in β single field [J]. Transactions of Nonferrous Metals Society of China, 2022, 32(9): 2889–2907.

## 增材制造异构组织 TiAl 合金热压缩过程中的 显微组织演变及动态再结晶机制

陶 慧1, 李慧中1,2,3, 李佳慧1, 王 丽2, 贺卫卫4, 谭孝芬1, 周 睿5, 梁霄鹏1,2,3

- 1. 中南大学 材料科学与工程学院,长沙 410083;
- 2. 中南大学 粉末冶金国家重点实验室,长沙 410083;
- 3. 中南大学 有色金属材料科学与工程教育部重点实验室, 长沙 410083;
  - 4. 西安赛隆增材技术股份有限公司, 西安 710016;
- 5. 香港城市大学 材料科学与工程系,香港高等研究院,香港九龙 999077

摘 要:采用热压缩实验、光学显微镜(OM)、扫描电镜(SEM)、电子背散射衍射(EBSD)和透射电镜(TEM)研究了电子束选区熔化(SEBM)制备的 Ti-48Al-2Cr-2Nb 合金(摩尔分数,%)在 1150  $\mathbb{C}$ 和 0.1 s<sup>-1</sup>条件下热变形过程中的显微组织演变和动态再结晶(DRX)机制。结果表明:合金的初始显微组织为沿打印方向交替分布的  $\gamma$  粗晶层和  $\gamma+\alpha_2+(\alpha_2/\gamma)$ 细晶层。热变形初期,粗晶中形成有利于后续变形的变形孪晶,细晶区域发生少量动态再结晶(DRX)。随着应变的增加,粗晶区和细晶区通过不同的再结晶机制形成大量的 DRX 晶粒。其中,细晶区的 DRX 机制为不连续动态再结晶(DDRX),粗晶区的 DRX 机制包括 DDRX 和连续动态再结晶(CDRX)。

关键词: TiAl 合金; 电子束选区熔化; 异构组织; 不连续动态再结晶; 连续动态再结晶

(Edited by Bing YANG)